coatings

MDPI

Article

Study on Wear Resistance of Nickel Cladding Layer with Imitation Shell Convex Strip Structure on the Surface of 7075 Aluminum Alloy Drill Pipe

Yan Zhao [1,2,3], Guorui Liao [1,2,3], Xu Li [1,2,3], Ke Gao [1,2,3,*], Congshan Zhang [1,2,3], Xiaoshu Lv [1,4,5], Hongxin Ai [1,2,3] and Xiaobo Xie [1,2,3]

[1] College of Construction Engineering, Jilin University, Changchun 130026, China
[2] Engineering Research Center of Geothermal Resources Development Technology and Equipment, Ministry of Education, Jilin University, Changchun 130026, China
[3] Key Laboratory of Drilling and Exploration Technology in Complex Conditions, Ministry of Natural Resources, Jilin University, Changchun 130026, China
[4] Department of Electrical Engineering and Energy Technology, University of Vaasa, P.O. Box 700, 65101 Vaasa, Finland
[5] Department of Civil Engineering, Aalto University, P.O. Box 12100, 02130 Espoo, Finland
* Correspondence: gaokenm@jlu.edu.cn

Abstract: In this study, a nickel cladding layer with a bionic convex strip structure was applied to the surface of an aluminum alloy drill pipe, and laser cladding technology was used to improve the wear resistance of the aluminum alloy drill pipe. Firstly, by observing the morphological characteristics of the shell surface, the ratio of the width of the convex strips to the spacing between the convex strips was obtained as 0.39–0.53, and thus a model of the bionic structure was constructed. Numerical simulations were performed, and the results showed that the wear of the bionic structure was reduced by 77.6% compared with that of the smooth structure. Subsequently, the cladding layers of both structures were coated on the drill pipe using nickel powder as the material, and wear tests were performed. The microstructure, composition, and hardness behavior of the cladding layers were analyzed using scanning electron microscopy, an X-ray diffractometer, and a microhardness tester. It was found that the cladding layer mainly consists of Al_3Ni_2, and there is a transition layer between the cladding layer and the aluminum alloy matrix, whose hardness is lower than that of Al_3Ni_2. In addition, the groove space can be formed between the convex strips, which effectively reduces the frequency of the debris flow. The results of the wear tests show that the wear of the cladding layer with the bionic structure is reduced by 74.0%. Similar results in numerical simulations and experiments verified that the designed cladding layer with a bionic convex strip structure can significantly improve the wear resistance of aluminum alloy drill pipes.

Keywords: laser cladding; shell bionics; simulation and testing; wear resistance

Citation: Zhao, Y.; Liao, G.; Li, X.; Gao, K.; Zhang, C.; Lv, X.; Ai, H.; Xie, X. Study on Wear Resistance of Nickel Cladding Layer with Imitation Shell Convex Strip Structure on the Surface of 7075 Aluminum Alloy Drill Pipe. *Coatings* **2023**, *13*, 1317. https://doi.org/10.3390/coatings13081317

Academic Editor: Vincent Ji

Received: 24 June 2023
Revised: 21 July 2023
Accepted: 25 July 2023
Published: 27 July 2023

1. Introduction

At present, drilling resources into deep resources is the general trend, and with the continuous increase in drilling depth, the requirements for drill pipes are getting higher and higher [1]. Aluminum alloy drill pipes have become a scientific optimization solution for designing ultra-deep well drill strings, due to their advantages such as light weight, low energy consumption, small bending stress, and strong corrosion resistance compared with traditional rigid drill pipes [2–4]. However, the development of aluminum alloy drill pipes is limited due to their poor tribological properties [5–7]. Therefore, it is necessary to improve their wear resistance.

Laser cladding technology is an emerging green technology that enables the production of high-performance coatings by controlling the material and process parameters of cladding. This technology plays a significant role in the remanufacturing and surface

strengthening of old parts [8–10]. Laser cladding has several advantages, such as a limited heat-affected zone, low dilution rate, small stress deformation, and fine coating microstructure. Additionally, it allows the use of high-quality coating materials with excellent physical and chemical properties, which can protect the surfaces of engineering components from wear, corrosion, thermal degradation, and impact during use [11–14]. From the above characteristics of laser cladding, it is a good idea to use laser cladding to improve the wear resistance of the aluminum alloy drill pipe surface. However, applying laser cladding to the entire surface of the component will increase the micro-movement wear, produce cracks and porosity, and affect the safe use of the components [15,16].

Bionics offer more accurate and intelligent solutions to engineering problems. After hundreds of millions of years of evolution, some organisms are capable of developing a number of body surface features with high abrasion resistance [17–19]. Yang et al. [20] analyzed the beetle body surface to design a cemented carbide drill with a bionic surface, which demonstrated better performance in reducing wear and jamming breakage. Chen et al. [21] designed a friction pad with a hexagonal structure imitating a tree frog foot pad and conducted friction tests. The test results showed that the hexagonal ring groove bionic structure could significantly improve the friction performance of the friction pad. Zhang et al. [22] developed a bionic drilling heat exchanger using circular grooves as the bionic unit. Numerical simulation results demonstrated a 13% reduction in fluid resistance. Pan et al. [23] used ANSYS software to perform finite element simulations of wear on unfolded wheels with microstructured and smooth structural surfaces, respectively. The simulation results showed that the life of microstructured surfaces was 26.5% longer than that of smooth surfaces.

From the above research status, we can see that aluminum alloy drill pipe has many advantages, but it also has the outstanding problem of poor wear resistance. The use of new parts can improve the surface wear resistance through laser-cladding technology, and the structural design of the cladding layer is crucial. Bionics can provide us with more accurate ideas to design certain structures to solve some problems more effectively. Therefore, this paper solves the problem of poor wear resistance in aluminum alloy drill pipes by designing the structure of the cladding layer by imitating the structural features of the shell surface. Then, laser cladding technology was used to form a nickel-cladding layer with a bionic structure on the surface of an aluminum alloy drill pipe. The results of the numerical simulations and wear tests show that the design of the bionic structure nickel-cladding layer can significantly improve the wear resistance of the aluminum alloy drill pipe. This also laid the foundation for the subsequent study.

2. Establishment and Numerical Simulation Analysis of Bionic Model

2.1. Selection and Measurement of Bionic Prototypes

The shell is the coat shell of a mollusk that lives near the water. As a common aquatic organism, the mollusk's shell has a regularly ordered surface texture that plays a unique role in reducing seawater abrasion. Its surface structure serves as an important reference for optimizing friction interfaces and is an ideal source of bionic inspiration [24]. Mollusks living near water are subjected to a large amount of frictional wear caused by collisions with other objects and impact wear caused by impact on water currents every day. In order to enhance the damage resistance strength of their shells, after a long period of evolution, mollusks gradually formed a convex prism-like body surface structure on the surface of their shells [25]. And there is a certain width of grooves between adjacent convex strips, separating the convex strips, as shown in Figure 1. (L is convex strips' width and D is spacing between convex strips).

In order to further study the morphological characteristics of the shell body surface, and then provide basic support for the subsequent numerical simulation and experimental processing, the image processing software ImageJ was used to measure the morphological characteristics of the body surface of the three shells. The relationship between the width of the convex strips and the spacing between the convex strips was found.

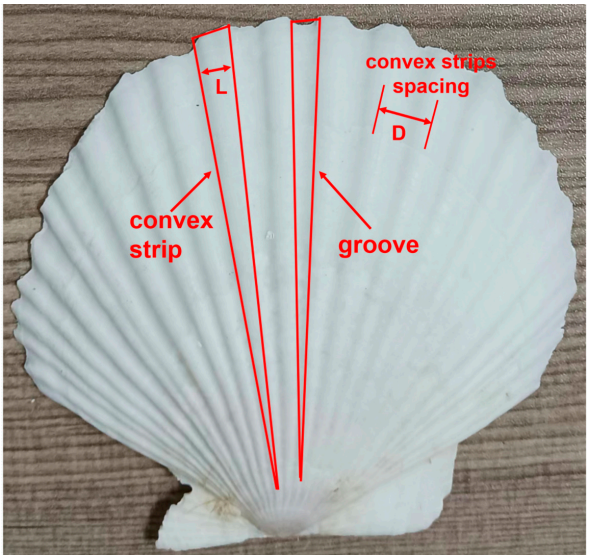

Figure 1. Convex strips and groove of a shell surface.

Three shells were collected from the Jiao he River in Jilin Province, each of slightly different sizes. The width of the convex strips and spacing size between the convex strips of each shell showed a clear bottom-up increasing trend, which can be divided into three areas: fine rib area, medium rib area, and coarse rib area, as shown in Figure 2.

Figure 2. Observation shells and their partitions.

The shells were first cleaned with water and alcohol to remove impurities, then fixed on the platform. A vernier caliper was placed above the shells, with the caliper size of 1 cm, and then a picture of the same frame of the caliper and the shell was taken. The picture was imported into ImageJ, and in the software, the line segment drawn by setting the caliper reading of 1 cm was set as the reference line segment. The arbitrarily drawn line segment could be scaled and identified according to the length of the 1 cm reference line segment and then the length of the drawn line segment was measured.

During the observation, the width and spacing of the convex strips in the I fine rib area, II medium rib area, and III coarse rib area of each shell were measured in several sets of data. A total of nine sets of data were obtained. The width and spacing of the convex strips in each set of data were averaged and the ratio of the two was obtained, as shown in Table 1. The average width of convex strips L was calculated with Equation (1) and the average spacing of convex strips D was calculated with Equation (2).

$$\overline{L} = \frac{L_1 + L_2 + \cdots + L_n}{n} \quad (1)$$

$$\overline{D} = \frac{D_1 + D_2 + \cdots + D_n}{n} \quad (2)$$

Table 1. Morphological characteristic parameters of shell surface.

Shell Number	Area	L (cm)	D (cm)	$\overline{L}$ (cm)	$\overline{D}$ (cm)	$\overline{L}/\overline{D}$
NO. 1	1-I	0.09, 0.10, 0.09, 0.07, 0.08	0.21, 0.23, 0.25, 0.21, 0.20	0.086	0.208	0.413
	1-II	0.27, 0.25, 0.24, 0.22, 0.27	0.53, 0.51, 0.56, 0.54, 0.60	0.250	0.548	0.456
	1-III	0.50, 0.51, 0.48, 0.53, 0.49	1.00, 1.01, 0.94, 1.03, 0.98	0.510	0.992	0.514
NO. 2	2-I	0.09, 0.13, 0.12, 0.10, 0.14	0.27, 0.26, 0.29, 0.27, 0.32	0.116	0.282	0.411
	2-II	0.32, 0.35, 0.39, 0.32, 0.41	0.78, 0.74, 0.81, 0.71, 0.80	0.358	0.768	0.466
	2-III	0.47, 0.61, 0.59, 0.67, 0.61	1.10, 1.14, 1.09, 1.13, 1.18	0.590	1.128	0.523
NO. 3	3-I	0.12, 0.10, 0.13, 0.11, 0.15	0.30, 0.35, 0.30, 0.28, 0.31	0.122	0.308	0.396
	3-II	0.35, 0.39, 0.33, 0.31, 0.40	0.77, 0.79, 0.69, 0.68, 0.71	0.356	0.728	0.489
	3-III	0.61, 0.58, 0.53, 0.64, 0.64	1.12, 1.09, 1.12, 1.15, 1.17	0.600	1.131	0.529

In the table, L: Convex strips width (cm) D: Convex strips spacing (cm), $\overline{L}$: Average width of convex strips (cm) $\overline{D}$: Average spacing of convex strips (cm).

Table 1 shows that the width of the convex strips in the I fine rib area is between 0.07 and 0.15 cm, and the spacing between the convex strips is between 0.2 and 0.35 cm. The width of the convex strips in the II middle rib area is between 0.22 and 0. 0.41 cm, and the convex strip spacing is between 0.5 and 0.8 cm. The width of the convex strips in the III coarse rib area is between 0.47 and 0.67 cm, and the convex strip spacing is between 0.95 and 1.2 cm. The average convex strip width, spacing, and the ratio of the nine sets of data are plotted in Figure 3. It can be seen that although there are differences in the average width and spacing of the convex strips in each group, the ratio between them is close. In the nine data sets, the ratio of the two ranged from 0.39 to 0.53, and the mean value of the ratio was 0.46.

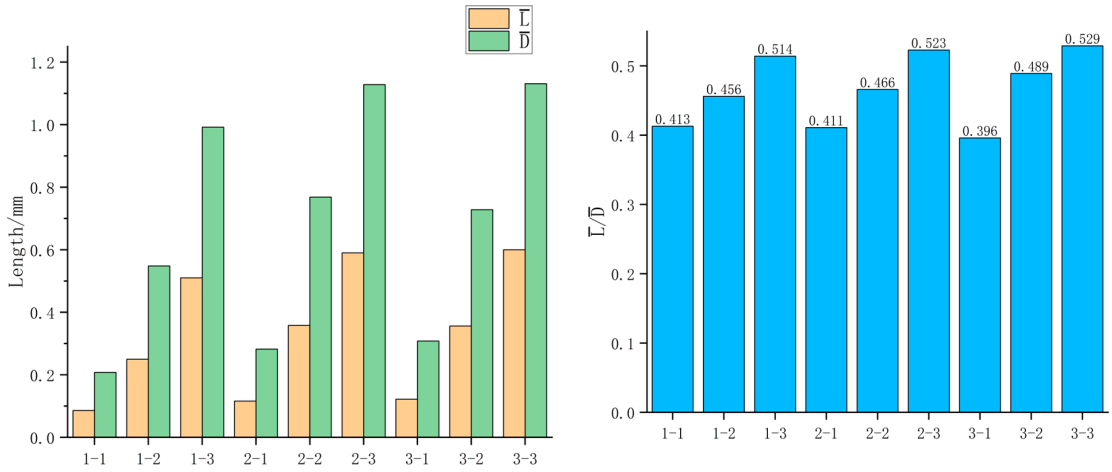

Figure 3. (**a**) Average width and average spacing of convex strips, (**b**) Ratio of the average convex strips' width to the average spacing.

2.2. Model Building and Material Definition

The measured ratio of the convex strips' width to the spacing between convex strips was applied to the model design of the wear layer of the aluminum alloy drill pipe used in the actual geological core drilling. And the material of the convex strips' structure was nickel (Ni) coating. The width of the convex strips is 2 mm, the spacing between convex strips is 4 mm and 5 mm, and the ratios of width and spacing are 0.5 and 0.4, respectively. The convex strips are arranged in parallel instead of the shell-shaped fan-shaped dispersion, which can effectively reduce the stress concentration phenomenon, as shown in Figure 4. A set of nickel coatings with a smooth structure was also designed as a control as shown in Figure 5.

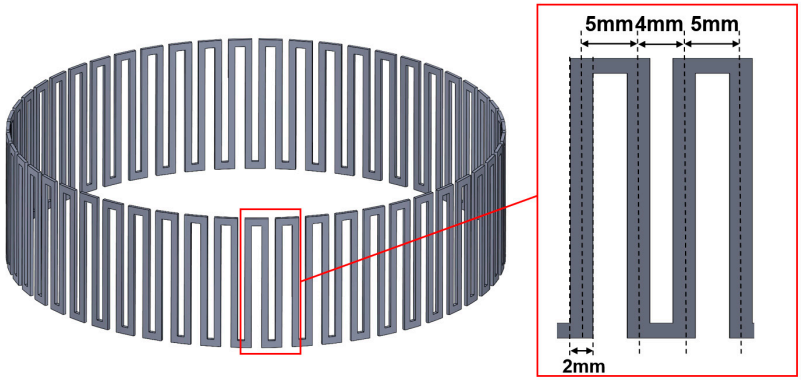

Figure 4. Parameters of convex strips structure nickel coating.

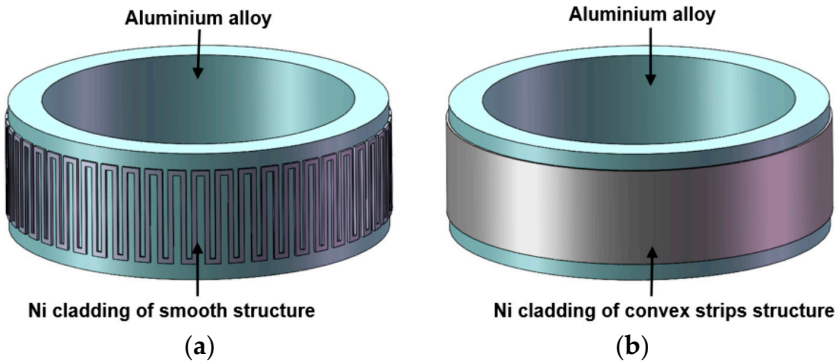

Figure 5. Two structures designed: (**a**) convex strip structure model, (**b**) smooth structure model.

The model parameters of the drill pipe were defined as having an outer diameter of 146 mm, a wall thickness of 13 mm, a nickel coating thickness of 1 mm, and a counter-ground granite rock sample thickness of 6 mm. The drill pipe was set to only rotate around the Y axis, with a load of 100 N applied to its inner wall. This limits all conditions of movement of the rock and imposes fixed constraints on it, as shown in Figure 6. The numerical simulation time was 0.1 s which was sufficient to see the comparison of stress distribution and wear amount of the two structures. The drill pipe rotation speed was 30 rpm. The material parameters for each component are listed in Table 2 [26–28].

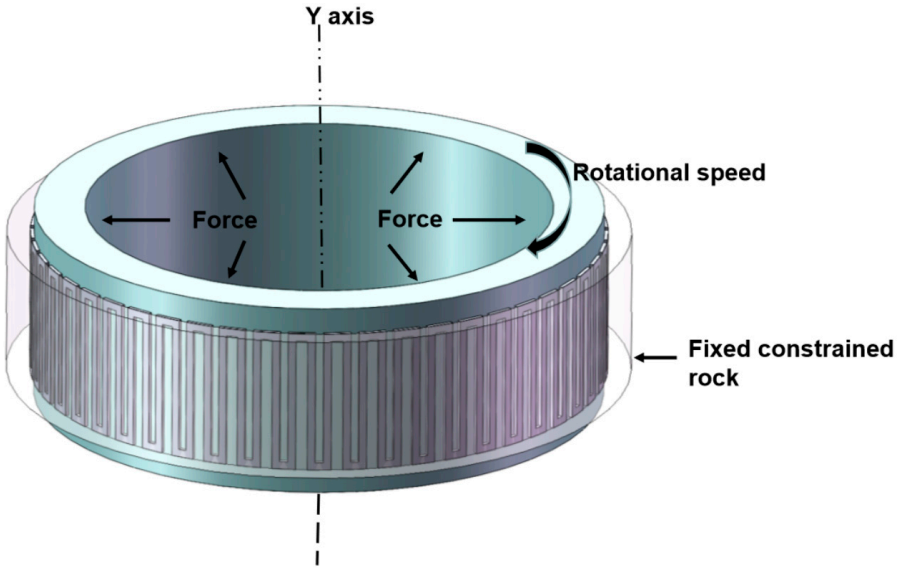

Figure 6. Models for numerical simulation.

Table 2. Material parameters of simulated parts.

Model Material	Density kg·m^{-3}	Elastic Modulus GPa	Poisson's Ratio
Ni	8900	210	0.3
Aluminum alloy	2810	72	0.33
Granite	2650	40	0.25

2.3. Mathematical Model of Wear

2.3.1. Archard Model

In the field of continuum mechanics, wear can be estimated using a phenomenological model that correlates different state parameters at the interface to material loss [29]. To approximate the material loss caused by wear, the finite element analysis software Ansys repositions the contact nodes on the contact surface. The amount of wear is estimated using the Archard model in the Ansys Mechanical platform.

The Archard wear model, which was established in 1953 by Archard based on the Holm model, provides a relationship between the wear rate and the contact pressure, material hardness, and sliding speed. The model is expressed as follows:

$$dV = \frac{KP^a {V_s}^b}{\sigma_s} ndt \tag{3}$$

In the formula:

V—wear volume;

P—contact load;

V_s—slipping speed between the contacting objects;

a—contact stress index;

b—speed index;

n—in-plane normal;

K—the wear coefficient, represented by the k value, ranges from 10^{-8} to 10^{-4} for slight wear and from 10^{-4} to 10^{-2} for severe wear;

σ_s—plastic yield stress for softer materials;

By assuming that the yield stress is equal to the hardness value, Equation (3) can replace the yield stress with the hardness (H). This allows for the Archard wear model expression to be rewritten as Equation (4):

$$dV = \frac{KP^a {V_s}^b}{H} ndt \tag{4}$$

H—The Brinell hardness of softer materials; the Brinell hardness of Ni is about 282.

The values of P and V_s are dependent on the boundary conditions, while k, a, and b need to be manually inputted. For this study, k is set at 1×10^{-6}, and a and b are both set at 1.

2.3.2. Wear Simulation Method

The wear simulation method workflow is depicted in Figure 7. It comprises two loops: condition setting and wear simulation. Prior to initiating the simulation, the setting conditions in the blue box need to be defined, which include pressure, velocity, and friction coefficient. As the simulation aims to compare two structures, the friction coefficient remains constant. In each iteration of the wear simulation loop, the contact nodes are repositioned, and nodal pressures, nodal velocities, and the relative displacements of each node along X, Y, and Z are computed. This is followed by the removal of material from the coated surface to represent wear. If the stable wear stage is reached, the iterative process stops [30]. Otherwise, it enters the next iterative cycle, as indicated in the purple process box.

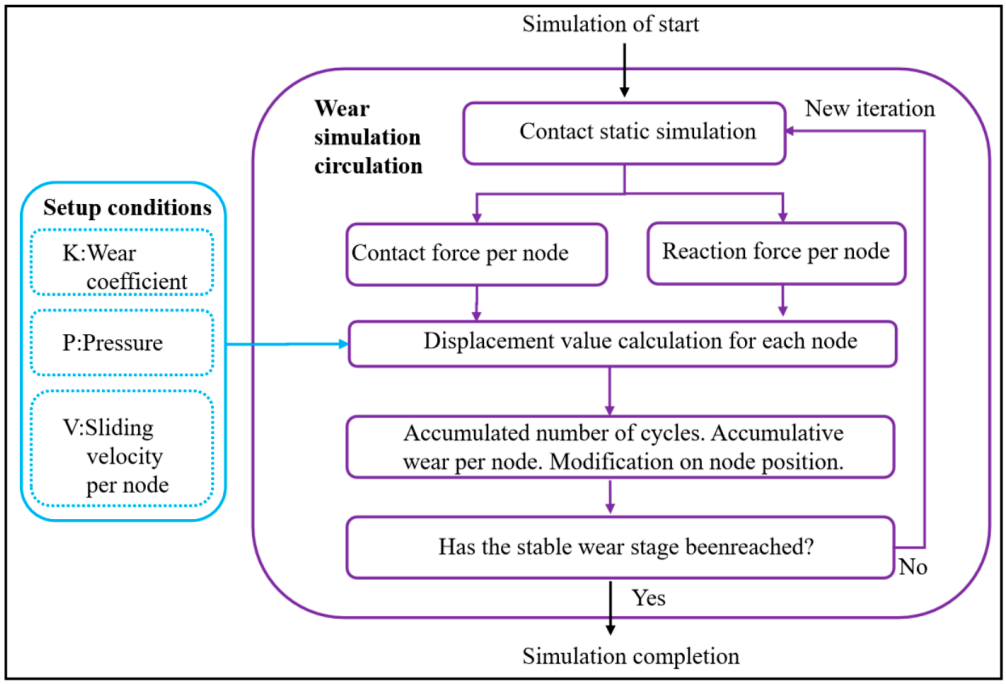

Figure 7. Simulation flow chart.

3. Experimental Section

3.1. Materials and Processing Used for Test Models

The test model comprises three components: surrounding rock, an aluminum alloy drill pipe, and two cladding layers with convex strips and a smooth structure, respectively. The aluminum alloy drill pipe used is 7075 grade, with an outer diameter of 146 mm, a wall thickness of 13 mm, and a height of 60 mm. The state of heat treatment of the 7075 aluminum alloy drill pipe is T6. The cladding layer is made of nickel powder with a particle size of 50–100 μm. The surrounding rock is granite. Table 3 shows the chemical composition of 7075 aluminum alloy and nickel powder.

Table 3. Chemical composition of 7075 aluminum alloy and nickel powder (wt.%).

Element	Zn	Mg	Cu	Fe	Cr	Si	Mn	Al	Ni	Tb
7075 aluminum alloy	5.63	2.35	1.64	0.35	0.22	0.09	0.02	Bal	-	0.02
Nickel powder	-	-	-	-	0.05	0.03	-	-	Bal	-

The nickel powder underwent vacuum-drying at a temperature of 150 °C for a duration of 2 h before the commencement of the test. The laser-cladding process was carried out using a CO_2 multifunctional CNC laser processing equipment with a flux of 15 L/min and a purity exceeding 99.9%. This equipment was composed of a fiber laser, a control system, and a cooling system. The laser model was JNM-1GY-300B Nd:YAG. Its output power was 300 W and scanning speed is 30 mm/min. The laser wavelength was 1064 nm and laser beam was Gaussian laser beam with divergence of less than 5 mrad. The cladding thickness of the two structures was 1 mm, and the cladding was relatively uniform. To coat the drill pipe with a layer of nickel cladding, the alloy surface was first ground with a grinding wheel to remove the oxide layer, then cleaned with acetone, and finally coated with a layer of light-absorbing material. Local heating of the aluminum alloy pipe's surface was carried out using a laser until it melted, and prefabricated nickel powder was quickly sprayed in front of the laser beam using a synchronous powder-feeding method. Once the beam was removed, the aluminum alloy cooled and solidified, forming a metallurgically bonded cladding layer on the outer layer of the aluminum alloy tube. By controlling the laser's

path, cladding layers of varying designs could be formed on the surface of the aluminum alloy drill pipe. The cladding principle is shown in Figure 8.

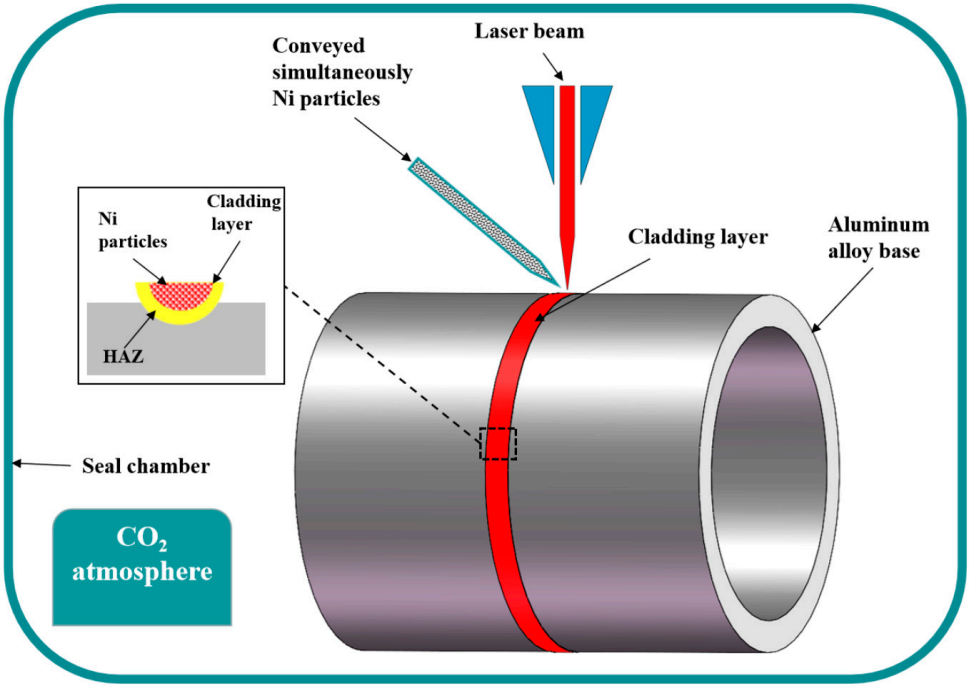

Figure 8. Principle diagram of laser cladding.

3.2. Wear Test

To further demonstrate the wear resistance of the convex strip structure cladding layer, a wear test bench was established as shown in Figure 9. The test bench can simultaneously perform friction and wear tests on both the bionic convex strip structure and the smooth structure, ensuring the consistency and reliability of the test. The two structures were tested three times each. The working principle of the test bench is depicted in Figure 10, and ω represents the rotational speed of the drill pipe.

(**a**) (**b**)

Figure 9. Abrasion test bench (**a**) Appearance of the test bench, (**b**) Wear parts installation.

During this wear test, the drill pipe was set to rotate at 50 r/min and a circumferential force of 1000 N was applied on the inner wall of the drill pipe. Drilling fluid is crucial in the actual drilling process. To make the test more realistic, clear water was used as the drilling fluid which continuously flushed the contact parts between the test parts. Each test period lasted 40 min. To minimize test errors, each group of tests was conducted three times and the average value was taken as the test result. The cladding layers' wear resistance of the two structures was evaluated by comparing the mass loss of the cladding layers.

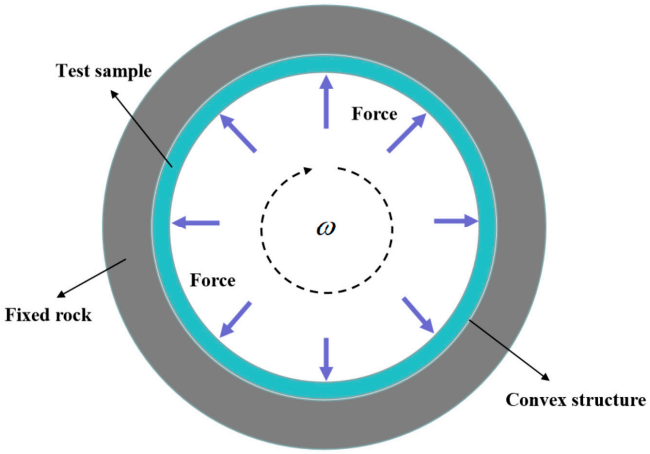

Figure 10. Working principle of the test bench.

3.3. Microstructural Characterization

After the sample was polished and cleaned, the sample was titrated and etched for 15 s using Keller reagent (1.0 mL HF + 1.5 mL HCl + 2.5 mL HNO_3 + 95 mL H_2O). Then, it was washed with anhydrous ethanol. German Zeiss Carl Zeiss-AxioImager A2m metallurgical microscope, Japanese Hitachi S4800 scanning electron microscope, and JSM-IT500A scanning electron microscope were used to observe the structure of the cladding layer and 7075 aluminum alloy substrate. Japan Rigaku D/Max2500C X-ray diffractometer was used for phase analysis of cladding layer. The Kα ray of Cu was used and the wavelength was 0.15418 nm. The scan range was 30°~80°.

3.4. Hardness Test

After the wear test, the test block was cut in the direction of the convex strips. A small test block was cut out for analysis and testing of the cladding layer. The test block was smoothed and polished using #400, #1000, #2000, and #5000 sandpaper and polishing cloth with alumina polishing liquid. Then, it was placed under HV1000 micro-Vickers hardness tester to test the hardness of the cladding layer, transition layer, coarse-grained region, and fine-grained region. A load of 1 kg was selected for the test and the loading time was 15 s. Each of the four areas was tested five times.

4. Results and Discussion

4.1. Simulation Results

4.1.1. Stress Distribution

At 0.1 s, the stress cloud images of the contact surface between the cladding layer and the rock of the two structures were extracted. As the cladding layer of the bionic structure is cyclical, analyzing a portion of the model can reflect the stress distribution characteristics and wear loss of the entire cladding layer ring. The direction of rotation of the drill pipe is clockwise under the top view perspective.

Figure 11 shows stress cloud images depicting the contact surface between the two structures and the rock. In Figure 11, it can be observed that the stress distributions of the cladding layers of the two structures at 0.1 s exhibit distinct characteristics. The stress distribution of the smooth cladding layer appears to be relatively uniform with no stress concentration phenomenon. The stress in the middle area is found to be smaller compared with the upper and lower edges. This is due to the fact that the edge area serves as the boundary of the cladding layer, leading to stress concentration when it makes contact with the rock. On the other hand, the stress of each convex strip in the cladding layer of the convex strip structure appears to be highly similar. Specifically, the edge stress on the side facing the rotation direction is greater than the edge stress on the back side, and both are greater than the stress in the middle area. Moreover, the stress on the upper and lower

edges is greater as compared with the stress in the middle area. More significant stress concentrations were observed at the ends of the upper and lower edges facing the direction of rotation. In addition, six stress measuring points a, b, c, d, e and f were selected in the stress cloud images of the two structures.

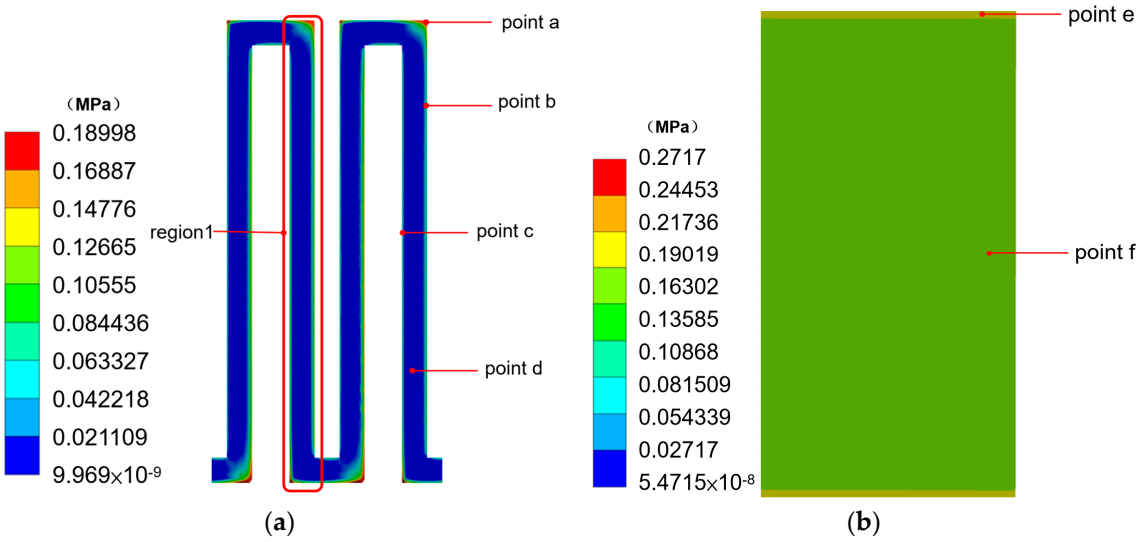

Figure 11. Stress clouds images at the contact surface of the two structures with the rock (**a**) Stress cloud images of convex strips structure, (**b**) Stress cloud images of smooth structure.

In order to further explore the stress distribution characteristics, the stress on each node in a convex strip region1 in Figure 11a is extracted, which is 37 mm long and 2 mm wide. Its bottom left end is used as the origin of the coordinates and the forward direction of rotation and vertical upward direction are, respectively, the positive direction of the X and Y axes. The position–stress scatter diagram is drawn as shown in Figure 12. The stress magnitudes of six points a, b, c, d, e, and f were also extracted and made into Table 4.

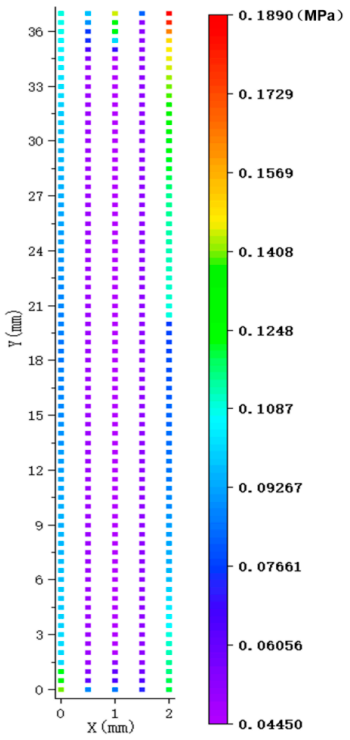

Figure 12. Region1 location stress–scatter diagram.

Table 4. Stresses of selected nodes in Figure 11a.

Location	a	b	c	d	e	f
Stress value (Mpa)	1.89×10^{-1}	9.94×10^{-2}	8.14×10^{-2}	4.33×10^{-2}	1.91×10^{-1}	1.68×10^{-1}

The stress analysis in Figure 12 reveals that stress is concentrated mainly on the upper and lower edges and the left and right edges of the convex strip, with relatively small stress in the middle area. The stress peak value is 4–5 times higher than the stress valley value. The stress distribution of the four points selected on the convex strip structure cladding layer shows that the stress at point a is the highest, which is four times that of point d. It indicates that stress concentration occurs at the end of the upper and lower edges facing the direction of rotation during the friction and wear process with the rock. Furthermore, the stress at point b is greater than that at point c, indicating that the edge on the side facing the direction of rotation generates greater stress on the same convex strip. The stress at point d is the smallest, indicating that the non-edge region of the convex strip structure cladding layer produces the least stress. The stress distribution of the two selected points on the smooth structure cladding layer is e > f, indicating that the stress generated on the upper and lower edges is greater than that in the middle area. In addition, the stress points e, a, and f are much larger than the stresses at points b, c, and d. This indicates that the stresses in the smooth structure are larger than the stresses in the convex structure, except for point a and the area similar to point a. The macroscopic expression is that the wear of the molten layer of the smooth structure is larger than that of the molten layer of the convex structure. The cause of this phenomenon is that during the rotation process, both Ni and Al alloys are in the elastic deformation stage, but the difference in elastic modulus between them is large, so the deformation variables will be different. Due to the continuous coating, the stresses in the smooth structure cannot be released and then stored in the coating. The convex strip structure breaks the continuous surface with grooves separating the convex strips, allowing space for stress to be released.

4.1.2. Comparison of Simulated Wear Volume Results

Table 5 presents the simulation results for the wear amount of the cladding layer after rotating for 0.1 s. Figure 13 displays the comparison of wear amounts between the two structures, where the blue column graph shows that the cladding layer with a convex strip structure has 77.6% less wear than the cladding layer with a smooth structure. In order to exclude the surface area change caused by the thickness change in the cladding layer, the amount of wear was divided by the external surface area of the model. The comparison of the wear depth of the two structures shown in the green bar graph in Figure 13 was obtained, which shows that the lifetime of the cladding layer of the convex strip structure is 64.8% higher than that of the smooth structure. This indicates that the design of the convex strip structure can effectively enhance the wear resistance and lifetime of the drill pipe.

Table 5. Wear results of numerical simulation.

Structure	0.1 s Wear Amount mm^3	Wear Rate mm^3/s	Wear Comparison	Model External Area mm^2	Wear Depth mm	Life Comparison
Smooth	1.54×10^{-9}	0.87×10^{-8}		14,209	1.08×10^{-13}	
Convex	3.44×10^{-10}	1.32×10^{-9}	77.6% reduction	9041	0.38×10^{-13}	64.8% improvement

4.2. Wear Test Results

4.2.1. Microstructure and Phase Composition of the Cladding Layer

Figure 14 shows the morphology of the aluminum alloy substrate, the transition layer, and the cladding layer observed under metallographic microscope after corrosion with a keller reagent. The microstructure of the transition layer between the cladding layer and the

aluminum alloy matrix was observed and analyzed using a scanning electron microscope with a larger magnification.

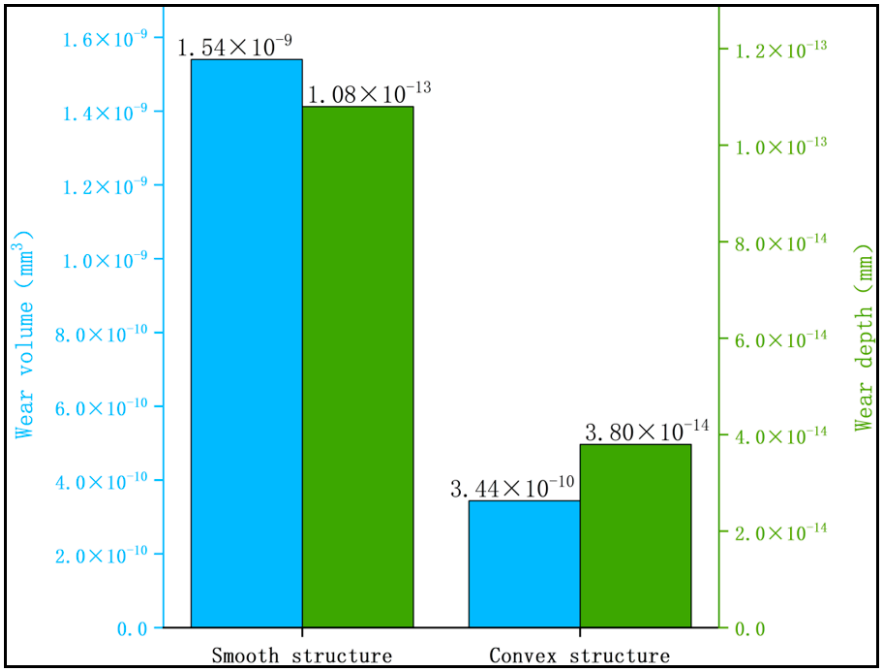

Figure 13. Comparison of wear volume and depth of wear of two structures.

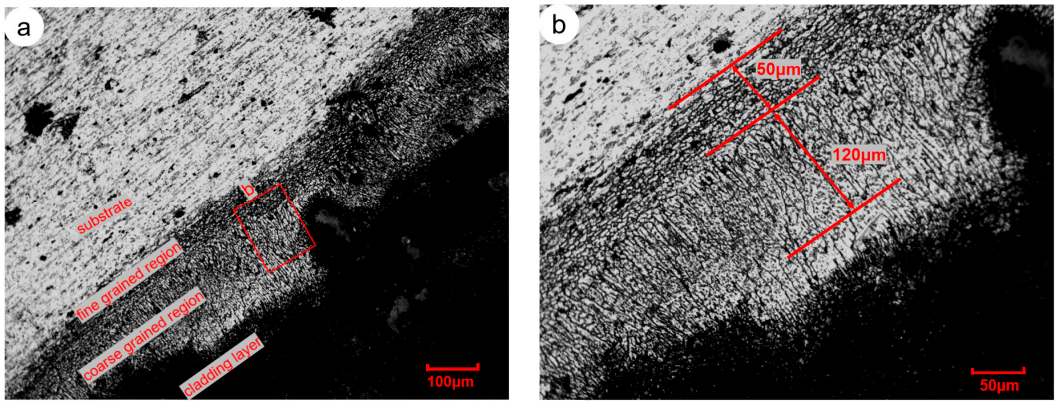

Figure 14. Transition layer under metallurgical microscope (**a**) External appearance of the transition layer, (**b**) Enlarged view of the transition layer.

Figure 15 shows a scanning electron micrograph of the aluminum alloy substrate transition layer and cladding layer. It can be seen from the Figure that there are significant differences in grain size and morphology between the fine-grained region and the coarse-grained region. The fine-grained region has equiaxed grains with sizes ranging from 3 to 10 μm, while the coarse-grained region has columnar grains with sizes ranging from 10 to 30 μm. Point A of the fine-grained region and point B of the coarse-grained region were selected for EDS spectroscopy to determine the composition of the coarse- and fine-grained regions. As shown in Figure 16, it can be seen that the composition of both points are aluminum and some impurities, which indicates that the cause of the coarse- and fine-grained regions is recrystallization and grain growth during the condensation of Al melting. The difference in grain size and morphological characteristics between the fine- and coarse-grained region is due to the fact that the fine crystalline zone produced by laser cladding is in contact with the aluminum alloy matrix, which is less affected by the heating of the laser and with the release of stored energy in the original grains; new equiaxed grains

without distortion are formed and grow, thus forming recrystallized grains. The coarse crystalline zone produced by laser cladding is closer to the cladding layer and is more affected by the heating, and the grains undergo the process of recrystallization and grain growth to form columnar crystals [31].

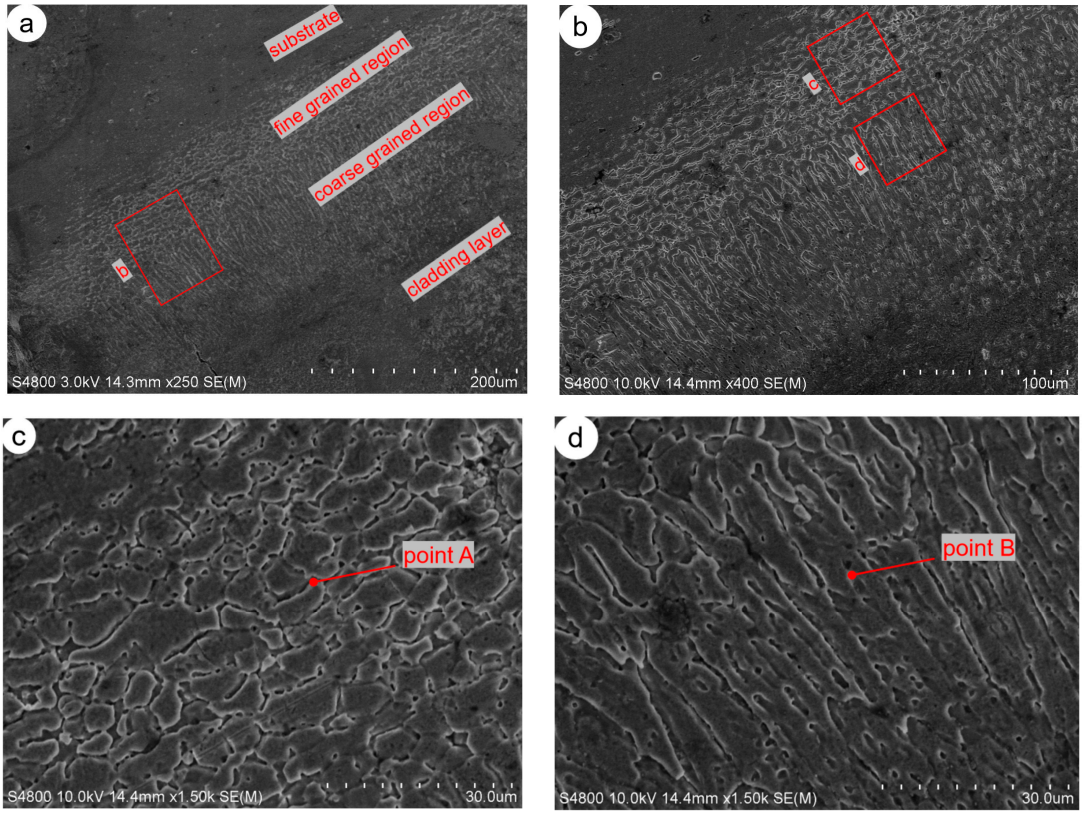

Figure 15. SEM micrograph (**a**) Substrate, transition layer, and cladding layer, (**b**) Transition layer, (**c**) Fine-grained region with EDS test point A, (**d**) Coarse-grained region with EDS test point B.

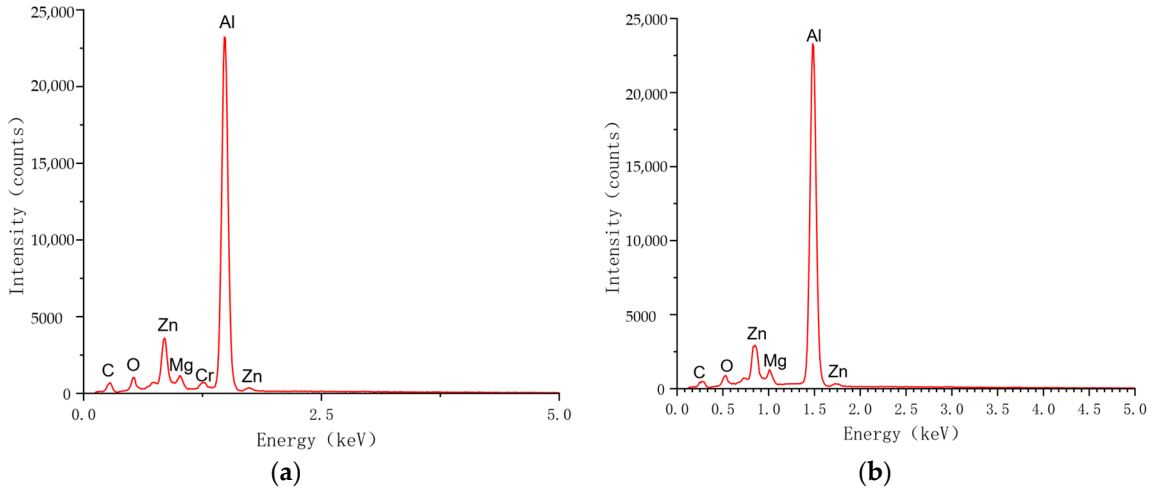

Figure 16. EDS spectral analysis of points A and B (**a**) EDS spectral analysis of point A, (**b**) EDS spectral analysis of point B.

Figure 17 shows the morphology of the cladding layer observed under the scanning electron microscope. It can be seen that the cladding layer is a uniformly distributed cast equiaxed crystal organization without the presence of Ni powder particles, and there are

small interstices within the cladding layer. The EDS spectral analysis of the selected C point on the cladding layer is shown in Figure 18, which shows that the main composition of the cladding layer is Al_xNi_y phase. Because the laser cladding is carried out in a CO_2 environment, there will be components such as C, O, etc. Because the impurities are entrapped in the nickel powder, there are components such as Si, Cr, etc.

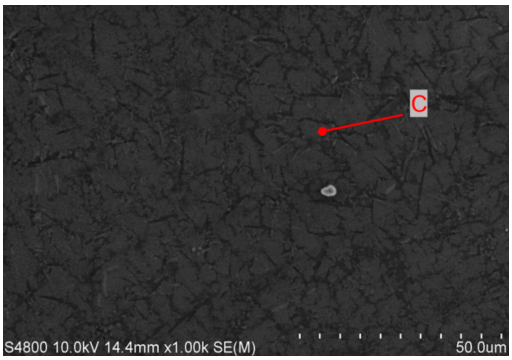

Figure 17. Microphotograph of cladding layer with EDS test point C.

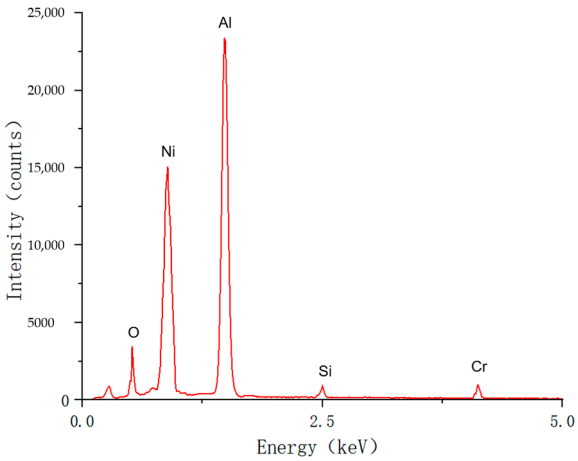

Figure 18. EDS spectral analysis of point C.

In order to better display the phase composition of each region, EDS mapping analysis was performed for the areas selected by the red boxes, as shown in Figure 19a. Figure 19b reflects element Ni enrichment, Figure 19c reflects element Al enrichment, and Figure 19d reflects element Zn enrichment. In the coarse-grained region, the fine-grained region, and the substrate, the main element is Al, and other elements are relatively few. The percentage of Al is large in these regions. Therefore, in the map, the brightness of Al in these regions is extremely bright. In the cladding layer, there are two main elements: Ni and Al. Therefore, the percentage of Al in this area is lower than in other brighter areas. Moreover, the brightness of the Al in the cladding layer contrasts with other areas where the Al is brighter, so it does not look obvious. But, the fact is that in the cladding layer, the elements Al and Ni are present at the same time. In areas outside the cladding layer, Ni hardly appears and Zn is enriched.

The composition of the cladding layer was derived from the EDS analysis of the cladding layer, and XRD analysis was performed to further investigate the specific products. Figure 20 shows the results of XRD analysis, and it can be concluded that the cladding layer mainly consists of Al_3Ni_2 and Al phase. The melting point of Ni is much higher than that of Al, and during the laser melting process, Al will melt in advance, and some of it will react with Ni to form Al_3Ni_2. In addition, Figure 20 shows that the diffraction peak of Ni does not correspond to that of the cladding layer, and there is no ferromagnetism on the surface of the molten layer, indicating that the Ni powder is no longer present and reacts

with Al to form Al_3Ni_2. Both the Al alloy matrix and the Ni powder were dissolved during the laser heating and cladding process. The chemical reaction during the melting process is as follows: 3Al+ 2Ni → Al_3Ni_2 [32,33].

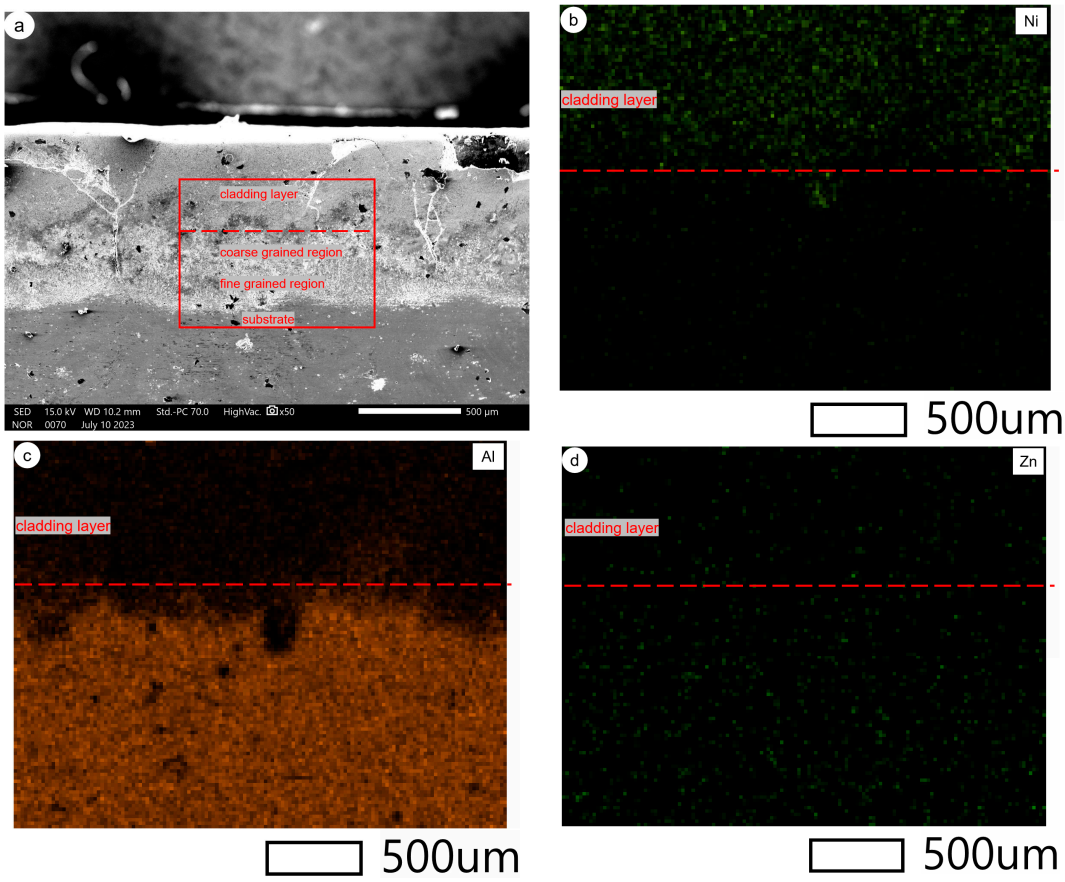

Figure 19. EDS mapping analysis: (**a**) regions of analysis: cladding layer, transition layer, coarse-grained region, and fine-grained region, (**b**) element Ni, (**c**) element Al, (**d**) element Zn.

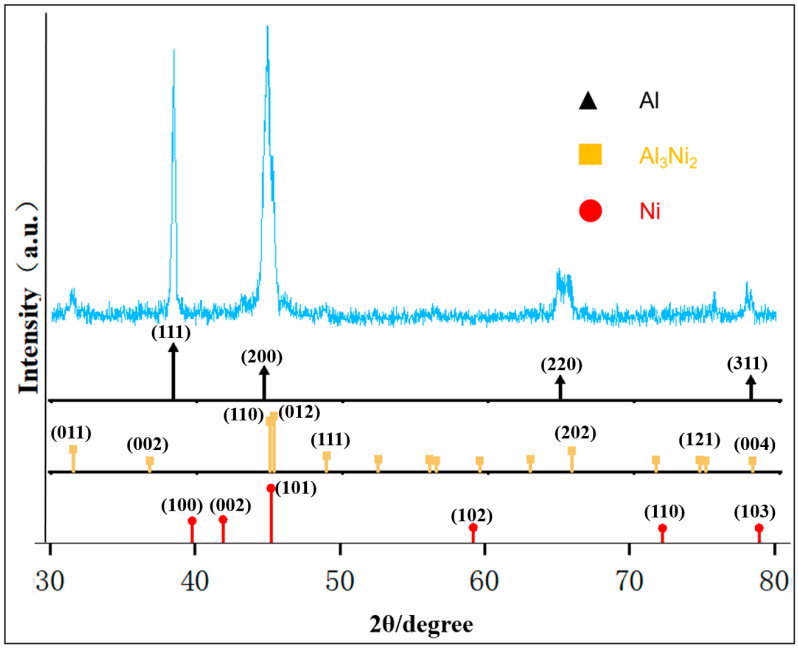

Figure 20. XRD analysis of cladding layer.

The reason why the drill pipe after laser cladding has better wear resistance is that Al_3Ni_2 produced in the melting process is an intermetallic compound with high hardness and wear resistance [34,35].The microhardness of the aluminum alloy matrix, fine-grained regions, coarse-grained regions, and cladding layer were tested in turn, and the results are shown in Figure 21. The hardness of the aluminum alloy matrix is 170 HV, and the hardness of the coarse- and fine-grained regions are 128 HV and 148 HV, respectively, which are 24.7% and 12.9% lower than the hardness of the matrix. The surface hardness of the cladding layer can reach 783 HV, which is 4.6 times the hardness of the substrate. When the drill pipe rotates and wears against the rock, the outer high-hardness Al_3Ni_2 as the hard phase has excellent resistance to deformation to reduce the wear. The transition layer and the aluminum alloy matrix as the soft phase can buffer the shear stress generated during the experiment.

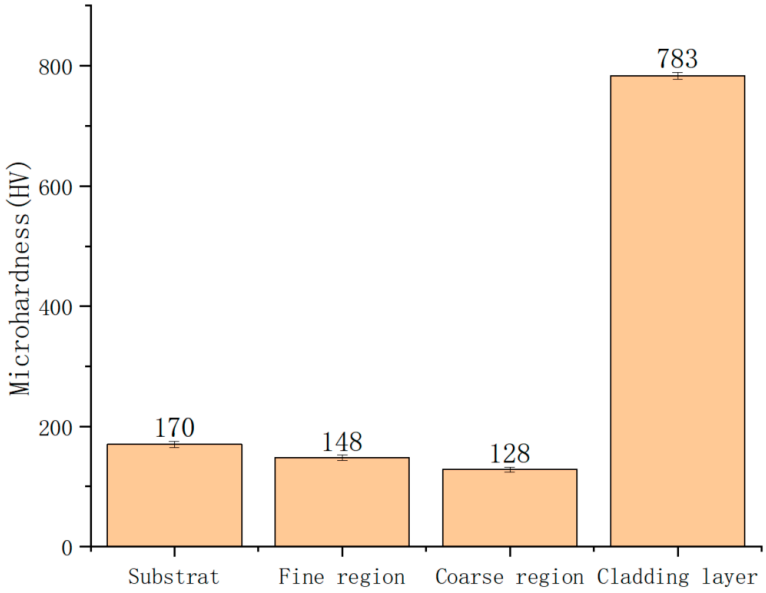

Figure 21. Microhardness of each area.

4.2.2. Results of Wear Test

The test results for the cladding layer of the bionic convex strips and smooth structures are shown in Table 6. The comparative results for the frictional wear quality of the two structures are shown in the blue bar graph in Figure 22. The blue bar graph shows that the wear quality of the cladding layer of the convex strip structure is reduced by 74.0% compared with that of the smooth structure. If ignoring the change in surface area due to the change in thickness of the cladding layer, the results of the comparison between the wear per unit areas of the two structures are shown in the green bar graph in Figure 22. The green bar graph shows that the lifetime of the convex strip structure is improved by 60% compared with the smooth structure. The experimental test results are close to the simulation results, indicating that the design of the convex strip structure can effectively improve the life of the drill pipe.

Table 6. Wear test results.

Structure	Experimental Wear g	Wear Comparison	Model External Area mm^2	Wear Per Unit Area g/mm^3	Life Comparison
Smooth	4.73		14,209	3.33×10^{-4}	
Convex	1.23	74.0%reduction	9041	1.36×10^{-4}	60.0%improvement

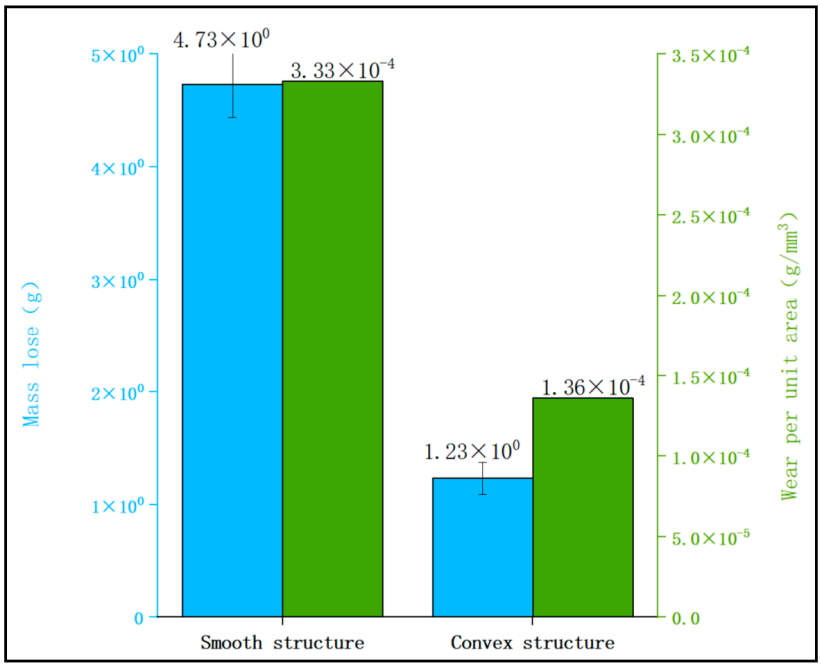

Figure 22. Comparison of wear volume and unit area wear volume of two structures.

Figure 23 shows the surface morphology of the cladding layer of the two structures after the wear test. It can be seen that the middle area of the cladding layer of the smooth structure is worn more uniformly, while the upper- and lower-side edges are worn more severely and there is an obvious peeling phenomenon. The convex strip structure is worn severely around the edges of each convex strip, and the middle area is worn more uniformly. The surface wear morphology of the two structures is consistent with the stress distribution in Figure 11, which illustrates the reliability of the numerical simulation.

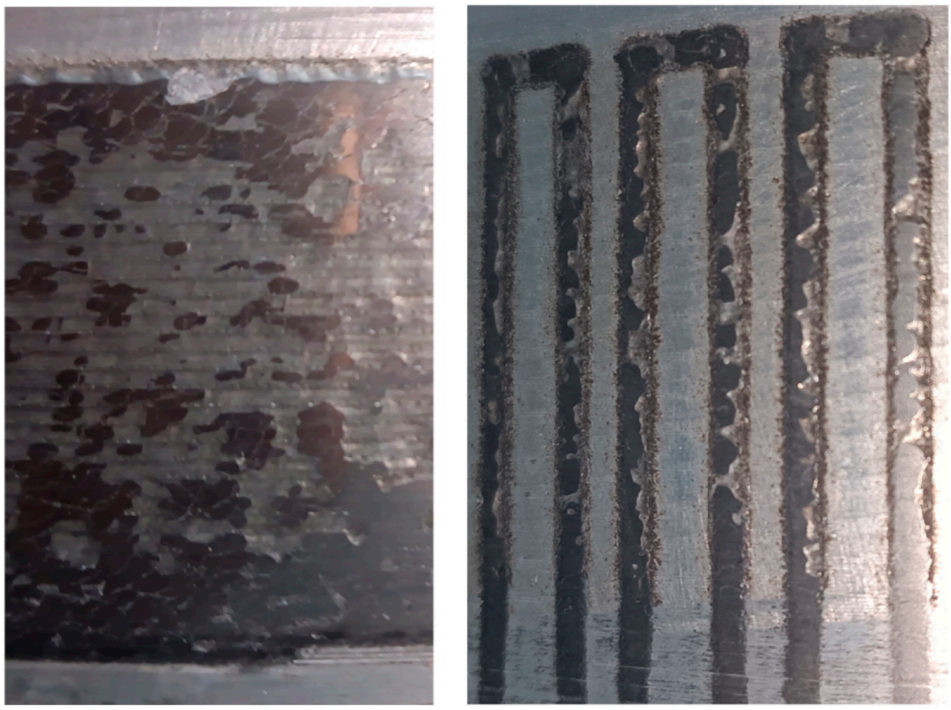

(**a**) (**b**)

Figure 23. Surface morphology of the test block after the test (**a**) smooth structure, (**b**) convex strip structure.

In addition, there are obvious scratches present in the smooth structure cladding layer, while there is no such phenomenon on the surface of the protruding convex strip structure. This is because the granules that are not washed off are sandwiched between the smooth structure cladding layer and the rock and wear with the cladding layer during the rotation process, and multiple abrasive wear occurs within the cladding layer. However, there is a groove structure between the protruding prism units of the convex strip structure, which can store the granules inside, effectively reducing the number of times the same granules rub against the cladding layer and reducing the abrasive wear, as shown in Figure 24.

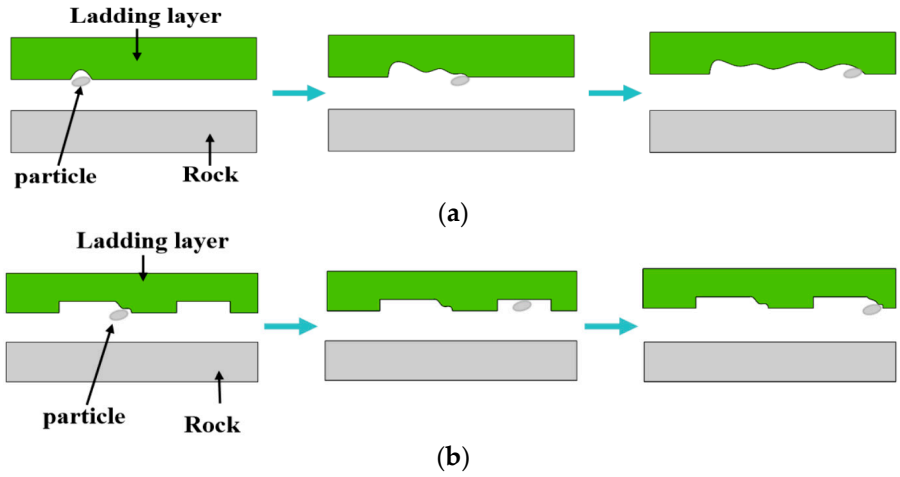

Figure 24. Abrasive wear comparison of two structures (**a**) smooth structure, (**b**) convex strip structure.

Based on the wear amount and surface morphology observed in the test results, it can be concluded that the bionic convex strip structure has a significant impact on enhancing stress distribution and prolonging the lifespan of the cladding layer.

5. Conclusions

In this paper, by observing and measuring the morphological characteristics of the shell surface, the relationship between the convex strips and the convex strips' spacing was obtained, followed by numerical simulations to analyze the stress distribution and wear of the bionic convex strip structure and smooth structure model against the rock; wear experiments were conducted and the following conclusions were finally obtained:

(1) By observing the morphological features on the body surface of several shells and measuring the convex strips and convex strip spacing, the ratio of the convex strips to the convex strips' spacing was obtained to be between 0.39 and 0.53;

(2) The bionic structure was designed according to the observed and measured data, and the stress distribution and wear amount of the bionic structure and the smooth structure were simulated and analyzed by using finite element software. The results show that the stress peak of the convex strip structure is significantly lower compared with the normal structure, the stress concentration phenomenon occurs at the edge of the convex strips, and the lifetime is improved by 64.8% compared with the smooth structure;

(3) The surface morphology of the melt layer of the two structures after the wear test is consistent with the stress distribution obtained from the simulation, and the overall life of the convex strips structure is improved by 60.0% compared with the smooth structure, which is close to the simulation results and verifies the accuracy of the finite element analysis results;

(4) The convex strip structure plays an important role in changing the original stress distribution, and at the same time, it can store the abrasive particles and reduce the abrasive wear phenomenon, thus improving the life of the clad layer and the life of the aluminum alloy drill pipe.

Author Contributions: Data curation, G.L. and X.L. (Xu Li); Project administration, Y.Z. and K.G.; Writing—original draft, G.L.; Writing—review and editing, G.L., C.Z., X.L. (Xiaoshu Lv), X.X. and H.A. All authors have read and agreed to the published version of the manuscript.

Funding: This research has been funded by the National Natural Science Foundation of China (Grant No. 41972324 and No. 42172345), the National Key R&D Program of China (Grant No. 2022YFC3005903-2), the Scientific Research Project of the Education Department of Jilin Province (Grant Nos. JJKH20221014KJ and JJKH20221016KJ), the Engineering Research Center of Geothermal Resources Development Technology and Equipment(Grant Nos. 23021 and 23022), Ministry of Education, Jilin University, and the Graduate Innovation Fund of Jilin University (Grant No. 2022104 and No. 2022245).

Institutional Review Board Statement: Not applicable.

Informed Consent Statement: Not applicable.

Data Availability Statement: Data are contained within the article.

Conflicts of Interest: The authors declare no conflict of interest.

References

1. Sun, Y.; Zhang, F.; Wang, Q.; Gao, K. Application of "Crust 1" 10k ultra-deep scientific drilling rig in Songliao Basin Drilling Project (CCSD-SKII). *J. Pet. Sci. Eng.* **2016**, *145*, 222–229. [CrossRef]
2. Kondrat'ev, S.Y.; Shvetsov, O.V. Technological and Operational Features of Drill Pipes from Aluminum Alloys 2024 and 1953. *Met. Sci. Heat Treat.* **2018**, *60*, 32–38. [CrossRef]
3. Liu, W.; He, W.; Jiang, H.; Wang, Q.; Chen, L.; Yang, Z.; Lin, Y. Influence of Graphene on Microstructure and Corrosion and Wear Resistance of Micro-Arc Oxidation Coatings on D16T Al Alloy Drill Pipe. *J. Mater. Eng. Perform.* **2021**, *30*, 4162–4173. [CrossRef]
4. Santus, C. Fretting Fatigue of Aluminum Alloy in Contact with Steel in Oil Drill Pipe Connections, Modeling to Interpret Test Results. *Int. J. Fatigue* **2008**, *30*, 677–688. [CrossRef]
5. Liu, J.; Yue, W.; Liang, J.; Hou, B.; Sun, J.; She, D.; Gu, Y.; Yi, P. Effects of evaluated temperature on tribological behaviors of micro-arc oxidated 2219 aluminum alloy and their field application. *Int. J. Adv. Manuf. Technol.* **2017**, *96*, 1725–1740. [CrossRef]
6. Liang, J.; Yue, W.; Gu, Y.; Liu, J.; Wang, C.; Ma, H. Improving Corrosion Resistance and Corrosive Wear Resistance of Aluminum Alloy Drill Pipe by Surface Nanocrystallization and Micro-arc Oxidation. *J. Mater. Eng. Perform.* **2018**, *27*, 4462–4472. [CrossRef]
7. Singh, M.; Mondal, D.; Das, S. Abrasive wear response of aluminium alloy–sillimanite particle reinforced composite under low stress condition. *Mater. Sci. Eng. A* **2006**, *419*, 59–68. [CrossRef]
8. Tian, F.J. Study on Microstructure and Properties of Slab Crystallizer by Laser Coaxial Cladding Strengthening. *Adv. Mater. Res.* **2011**, *189–193*, 3692–3696. [CrossRef]
9. Ji, X.; Luo, C.; Sun, Y.; Zhao, J. Corrosive wear of multi-layer Fe-based coatings laser cladded from amorphous powders. *Wear* **2019**, *438–439*, 203113. [CrossRef]
10. Zhang, H.; Chong, K.; Zhao, W.; Sun, Z. Laser cladding in-situ micro and sub-micro/nano Ti-V carbides reinforced Fe-based layers by optimizing initial alloy powders size. *Mater. Lett.* **2018**, *220*, 44–46. [CrossRef]
11. Song, B.; Yu, T.; Jiang, X.; Xi, W.; Lin, X. Development mechanism and solidification morphology of molten pool generated by laser cladding. *Int. J. Therm. Sci.* **2020**, *159*, 106579. [CrossRef]
12. Cheng, Y.-H.; Cui, R.; Wang, H.-Z.; Han, Z.-T. Effect of processing parameters of laser on microstructure and properties of cladding 42CrMo steel. *Int. J. Adv. Manuf. Technol.* **2017**, *96*, 1715–1724. [CrossRef]
13. Farayibi, P.K.; Abioye, T.E.; Clare, A.T. A parametric study on laser cladding of Ti-6Al-4V wire and WC/W2C powder. *Int. J. Adv. Manuf. Technol.* **2016**, *87*, 3349–3358. [CrossRef]
14. Huang, F.; Jiang, Z.; Liu, X.; Lian, J.; Chen, L. Microstructure and properties of thin wall by laser cladding forming. *J. Mater. Process. Technol.* **2009**, *209*, 4970–4976. [CrossRef]
15. Ding, J.; Leen, S.B.; McColl, I.R. The effect of slip regime on fretting wear-induced stress evolution. *Int. J. Fatigue* **2004**, *26*, 521–531. [CrossRef]
16. Xu, Z.; Li, D.; Lu, Z.; Lv, X.; Liu, Y.; Liu, J.; He, C. Study on the fretting wear behavior over a wide temperature range of an Inconel 718 superalloy deposited by laser cladding. *Eng. Fail. Anal.* **2023**, *143*, 106864. [CrossRef]
17. Vincent, J.F. Biomimetics—A Review. *Proc. Inst. Mech. Eng. H* **2009**, *223*, 919–939. [CrossRef]
18. Yu, H.; Shao, L.; Zhang, S.; Zhang, J.; Han, Z. An innovative strategy of anti-erosion: Combining bionic morphology and bionic arrangement. *Powder Technol.* **2022**, *407*, 117653. [CrossRef]
19. Ge-Zhang, S.; Cai, T.; Yang, H.; Ding, Y.; Song, M. Biology and nature: Bionic superhydrophobic surface and principle. *Front. Bioeng. Biotechnol.* **2022**, *10*, 1033514. [CrossRef]
20. Yang, X.; Xia, R.; Zhou, H.; Guo, L.; Zhang, L. Bionic surface design of cemented carbide drill bit. *Sci. China Technol. Sci.* **2015**, *59*, 175–182. [CrossRef]

21. Chen, D.; Zhang, Y.; Long, G.; Liu, W.; Li, X.; Sun, Y.; Chang, Z. An Optimal Wet Friction Plate Inspired by Biological Surface Patterns. *J. Bionic Eng.* **2018**, *15*, 872–882. [CrossRef]
22. Zhang, J.; Liu, Y.; Qin, X.; Dou, Z.; Meng, Q.; Xu, X.; Lv, J. Optimization design and drag reduction characteristics of bionic borehole heat exchanger. *Front. Energy Res.* **2022**, *10*, 1024623. [CrossRef]
23. Pan, C.; Chang, J.; Wang, C.; Gu, Y. Study on microstructure wear reduction performance and life prediction of unfolding wheel. *J. Mech. Sci. Technol.* **2022**, *36*, 1397–1405. [CrossRef]
24. Wang, H.; Lin, N.; Yuan, S.; Liu, Z.; Yu, Y.; Zeng, Q.; Li, D.; Fan, J.; Wu, Y. Numerical simulation on hydrodynamic lubrication performance of bionic multi-scale composite textures inspired by surface patterns of subcrenata and clam shells. *Tribol. Int.* **2023**, *181*, 108335. [CrossRef]
25. Zhang, H.; Zhang, P.; Sui, Q.; Zhao, K.; Zhou, H.; Ren, L. Influence of Multiple Bionic Unit Coupling on Sliding Wear of Laser-Processed Gray Cast Iron. *J. Mater. Eng. Perform.* **2017**, *26*, 1614–1625. [CrossRef]
26. Zhang, C.; Gao, K.; Zhao, Y.; Xie, X.; Zhang, C.; Lv, X. Simulation and Experimental Study on Rock-Breaking Mechanism of the Reverse Rotary Torque Self-balancing Dual Drill Bit. *Arab. J. Sci. Eng.* **2023**, 1–16. [CrossRef]
27. Liu, X.; Zhou, S.; Yan, Z.; Zhong, Z.; Shikazono, N.; Hara, S. Correlation between microstructures and macroscopic properties of nickel/yttria-stabilized zirconia (Ni-YSZ) anodes: Meso-scale modeling and deep learning with convolutional neural networks. *Energy AI* **2021**, *7*, 100122. [CrossRef]
28. Wang, X.; Liu, B.; Gao, K.; Meng, Q.; Sun, Y. Analysis of thermal deformation and influencing factors in shrink-fitting assembly of aluminum alloy drill pipe. *Adv. Mech. Eng.* **2016**, *8*, 1–15. [CrossRef]
29. Rajesh, A.M.; Doddamani, S.; Mohamed, K.K.; Bharath, K.N. Dry sliding wear simulation of hybrid aluminum metal matrix composites. *Adv. Compos. Hybrid Mater.* **2020**, *3*, 120–126. [CrossRef]
30. Rezaei, A.; Van Paepegem, W.; De Baets, P.; Ost, W.; Degrieck, J. Adaptive finite element simulation of wear evolution in radial sliding bearings. *Wear* **2012**, *296*, 660–671. [CrossRef]
31. Liu, Y.; Wang, Y.; Xu, X.; Hopper, C.; Dong, H.; Wang, X.; Zhu, H.; Jiang, J. The study of hot deformation on laser cladding remanufactured 316L stainless steel. *Mater. Des.* **2021**, *212*, 110255. [CrossRef]
32. Sallamand, P.; Pelletier, J.M. Laser Cladding On Aluminum-Base Alloys—Microstructural Features. *Mater. Sci. Eng. A-Struct. Mater. Prop. Microstruct. Process.* **1993**, *171*, 263–270. [CrossRef]
33. Parsa, M.; Soltanieh, M. On the formation of Al3Ni2 intermetallic compound by aluminothermic reduction of nickel oxide. *Mater. Charact.* **2011**, *62*, 691–696. [CrossRef]
34. Krasnowski, M.; Gierlotka, S.; Kulik, T. Al3Ni2–Al composites with nanocrystalline intermetallic matrix produced by consolidation of milled powders. *Adv. Powder Technol.* **2014**, *25*, 1362–1368. [CrossRef]
35. Vojtěch, D.; Novák, M.; Zelinková, M.; Novák, P.; Michalcová, A.; Fabián, T. Structural Evolution of Electroless Ni–P Coating on Al–12 Wt.% Si Alloy During Heat Treatment at High Temperatures. *Appl. Surf. Sci.* **2009**, *255*, 3745–3751. [CrossRef]